Progress In Electromagnetics Research B, Vol. 100, 19–38, 2023

A Metallic 3D Printed Modularized Dual-Stopband AMC-Loaded Waveguide Slot Filtering Antenna

Xingyu Cui and Bing Zhang*

Abstract—A 3D printing and printed circuit board (PCB) hybrid fabricated modularized dual-stopband artificial magnetic conductor (AMC)-loaded filtering antenna is proposed for an X-band high-power radar system. By loading low-cost microstrip AMCs of different frequency responses into a waveguide slot array, we achieve a modularized filtering antenna whose frequency response can be simply controlled by replacing different AMCs. The waveguide slot array only works as a fixture to host different AMCs to achieve various filtering antenna frequency responses. The interchangeable modularized design helps to reduce the difficulty and cost of component fabrication by eliminating the need for complex resonant cavities inside the waveguide filtering antenna, which is time-efficient at the stage of product prototyping when numerous iterations are needed on a trial-and-error base. A dual-stopband filtering antenna is designed and fabricated in the X-band to verify the design concept. The passband covers 9.25–10.6 GHz with the passband gain greater than 10 dBi. The antenna radiates frequency-dependent scanning beams in the passband. The stopbands are 8.1–9 GHz and 10.75–11.5 GHz, and the out-of-band rejection is larger than 35 dB. The proposed design concept provides a different thought to achieve a low-cost filtering antenna by using interchangeable modularized components. The fabricated antenna prototype is a capable candidate for high-power airborne radar applications.

1. INTRODUCTION

Metamaterials have physical properties that natural materials do not possess, such as the artificial magnetic conductor (AMC), high impedance surface (HIS), and negative refractive index material [1–4]. Metamaterials achieve special physical properties through their complex structures, which allow the control of the electrical parameters and spatial electromagnetic (EM) field distribution. Ziolkowski and Erentok designed a metamaterial spherical shell with a negative uniform isotropic permittivity and placed an electric small dipole antenna inside the metamaterial shell, in which the metamaterial shell and electric small dipole formed a resonance and obtained a very high radiation efficiency [1]. Efforts have also been taken to planarize metamaterials. To simplify the structure of metamaterials, [5–8] established the concept of generalized sheet transition conditions (GSTC) and introduced a series of analytical foundations for metasurfaces. The metasurface, as a planar equivalent alternative to the metamaterial, can achieve special physical properties in a planar structure. A variety of planar antennas incorporating metasurfaces were proposed [9–13]. A Huygens metasurface was designed to reduce 50% of the beam squinting in a leaky wave antenna [9]. Vallecchi et al. proposed a high-impedance surface to achieve a low-profile folded dipole antenna with a gain of up to 7 dBi [10]. The nature of the metasurface is to tune the propagation constant by resonant structures for desired frequency response. The low profile of its planar geometry allows it to be widely used in planar structures. However, the combination of antennas with a three-dimensional structure and metasurface of a two-dimensional structure is not very common.

Received 6 February 2023, Accepted 16 March 2023, Scheduled 15 April 2023
* Corresponding author: Bing Zhang (bzhang0609@hotmail.com).
The authors are with the College of Electronics and Information Engineering, Sichuan University, Chengdu 610065, P. R. China.

The waveguide slot array antenna with high efficiency, high power capacity, and high mechanical strength is suitable for high-power applications such as airborne radar [14–29]. Waveguide slot array antennas reported in [14–17] feature various properties, such as circular polarization [14–16], dual-band [17, 18], low sidelobe [19–21], and high efficiency [22–25]. In a highly integrated airborne radar system, the normal operation of the receiver is prone to be affected by the high-power transmitted electromagnetic waves from the transmitter due to the limited spacing between the receiving and transmitting antennas. So, a filtering function is needed to ensure good isolation between the transmitter and receiver. To solve this problem, T-shaped cavity bandpass and bandstop filters were integrated into the waveguide feeding network [26, 27]. The filtering function was achieved at the cost of an increased antenna footprint from the enlarged feeding network, which also gave rise to the decreased antenna gain. To make the waveguide slot array antenna more compact while keeping the filtering function, a grating metal sheet-loaded waveguide slot array antenna was proposed with a filtering frequency response [28]. The bottom electric wall of the waveguide was converted into a magnetic wall by loading metasurfaces to achieve the filtering response [29, 30]. These methods achieved good filtering responses, but their roll-off bands between the stopband and passband were as wide as 1.25 GHz in [28], 2.4 GHz in [29], and 1.1 GHz in [30], respectively, which led to their inability to be used in scenarios where the transmitter's and receiver's operational frequencies were very close. In addition, since they only implemented one single stopband, they cannot be used for multiband applications as shown in Fig. 1.

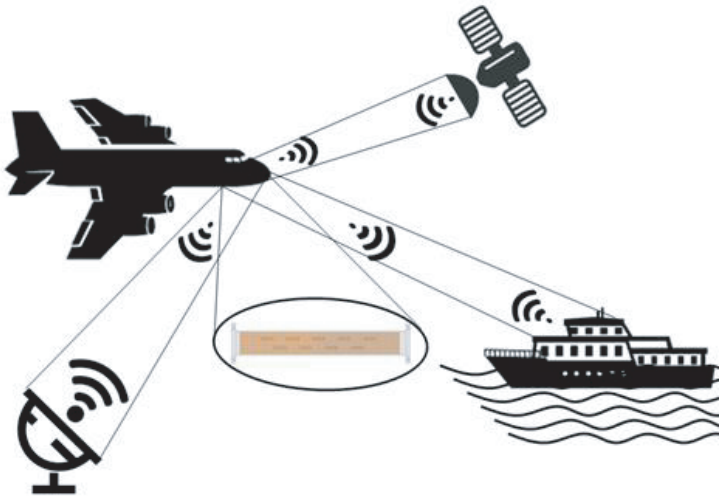

Figure 1. Application scenario of the multiband wireless communication and airborne radar of an aircraft.

This paper proposes a low-cost modularized waveguide slot array filtering antenna with a dual-stopband. The metallic 3D printed waveguide slot array is loaded with a microstrip AMC, which provides a good dual-band frequency response. For the planar structure of the microstrip AMC, the filtering frequency response is achieved at a negligible footprint cost of the device. Through calculation, the AMC causes an upshift of the waveguide's cutoff frequency. By designing a dual-band AMC whose operational frequencies coincide with the cutoff frequency of the AMC-loaded waveguide, two stopbands are formed, and a passband is achieved between the two stopbands. The steep roll-off of the AMC's frequency response is also reflected in the antenna's frequency response. The proposed design concept discards the traditional complex resonant cavities in waveguide filtering antenna, which requires sophisticated processes to fabricate. The low-cost interchangeable microstrip AMC by PCB process reduces the antenna's fabrication cost. The waveguide slot array functions as the AMC's fixture, by which various frequency responses can be easily achieved by just inserting different AMCs into the waveguide. The design concept can also be extended to multi-port devices to achieve a multi-stopband filtering response, which is desirable for a multiband highly integrated system. The novelty of the proposed work lies in its dual-stopband filtering frequency response, the steep roll-off between the passband and stopband, the modularized interchangeable design, and the low-cost by hybrid use of

metallic 3D printing and PCB fabrication technologies. The paper is organized as follows. Section 2 introduces the design and analysis of the proposed antenna. Section 3 verifies the characteristics of the antenna by simulation and measurement. Section 4 concludes the paper.

2. ANTENNA DESIGN AND ANALYSIS

2.1. Design of the Proposed Antenna

The geometry of the proposed antenna is shown in Fig. 2. It consists of a slotted waveguide and a dual-band AMC fabricated on a Rogers RO4003C substrate. The waveguide is a standard WR-90 waveguide with an FBM-100 flange made by the metallic 3D printing technology selective laser melting (SLM) using aluminum alloy. The short turn-around time and low cost of 3D printing technology are much valued at the early stage of device prototyping, which requires frequent fabrications on a trial-and-error base. The radiating slot on the top wall of the waveguide is 15.5 mm long and 2.5 mm wide, with a 15 mm spacing. Ridges to fix the AMC substrate are designed on the magnetic wall of the waveguide. The microstrip AMC is placed directly on the bottom wall of the waveguide. The top metal layer of the AMC consists of two forms of AMC unit cells periodically arranged. The dielectric layer has a dielectric constant of 3.55, a loss angle tangent of 0.0027, and a thickness of 0.813 mm, with periodically distributed conductive via holes connecting the upper metal layer and bottom ground plane. The bottom layer is a metallic ground plane, which is in close contact with the bottom electric wall of the waveguide. The length of the PCB is slightly shorter than the length of the waveguide to

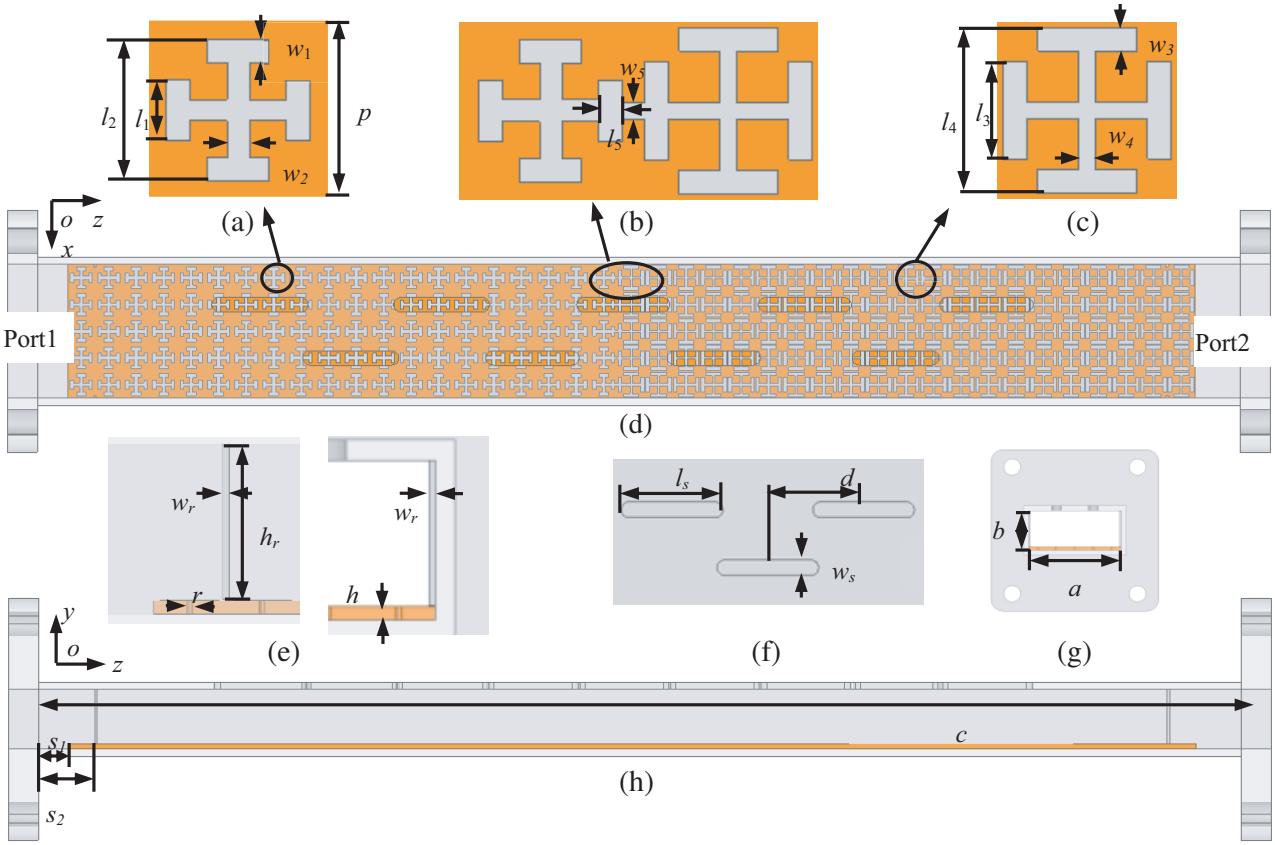

Figure 2. Geometry of the proposed antenna: (a) high-frequency AMC unit cell, (b) AMC junction, (c) low-frequency AMC unit cell, (d) top view of the proposed antenna, (e) zoomed side view of the ridge in the waveguide to fix the AMC, (f) radiating slots, (g) waveguide flange, and (h) side view of the proposed antenna.

Table 1. Geometric parameters of the proposed antenna.

Symbols	Parameters	Value (mm)
a	width of the waveguide slot array	22.86
b	height of the waveguide slot array	10.16
c	length of the waveguide slot array	210
d	spacing between radiating slots	15
h	thickness of the AMC substrate	0.81
h_r	height of the ridge to fix AMC	9.25
l_1	stub length of the high-frequency AMC unit cell	3.7
l_2	arm length of the high-frequency AMC unit cell	1.6
l_3	stub length of the low-frequency AMC unit cell	4.3
l_4	arm length of the low-frequency AMC unit cell	2.4
l_5	length of the AMC junction	0.67
l_s	length of the radiating slot	15.5
l_r	length of the ridge	0.4
p	cell size of the AMC unit	4.57
r	radius of the conductive via	0.2
s_1	offset of the AMC to the flange	10
s_2	offset of the ridge to the flange	14.57
w_1	stub width of the high-frequency AMC unit cell	0.6
w_2	arm width of the high-frequency AMC unit cell	0.6
w_3	stub width of the low-frequency AMC unit cell	0.6
w_4	arm width of the low-frequency AMC unit cell	0.4
w_5	arm width of the AMC junction	0.4
w_s	width of the radiating slot	2.4
w_r	width of the ridge	0.7

protect the edges of the PCB from wear and tear when the antenna is connected with other devices on the waveguide flange interface. The geometric parameters of the proposed antenna are listed in Table 1.

2.2. Analysis of the Proposed Antenna

2.2.1. Single-Frequency AMC

The cutoff frequency of a waveguide can be determined by Maxwell's equations and boundary conditions. After changing the bottom wall of the waveguide to perfect magnetic conductor (PMC), the boundary conditions and cutoff frequency change. Therefore, by taking the new boundary conditions into Maxwell's equations, we can obtain the final solution of the magnetic field in the z-direction of the waveguide with the bottom wall as PMC as shown in Eq. (1). The specific calculation procedure is given in the Appendix.

$$H_z(x,y,z) = A_{mn}\cos\frac{m\pi x}{a}\sin\frac{(2n+1)\pi y}{2b}e^{-j\beta z} \tag{1}$$

The cutoff frequency of the PMC-loaded waveguide can be calculated as

$$f_c = \frac{1}{2\pi\sqrt{\mu\varepsilon}}\sqrt{\left(\frac{m\pi}{a}\right)^2 + \left(\frac{(2n+1)\pi}{2b}\right)^2} \tag{2}$$

As can be seen from Eq. (2), the cutoff frequency of the PMC-loaded waveguide is higher than that of a common waveguide, indicating the upshift of the operational band of the waveguide when loaded with a PMC.

To mimic the boundary condition of PMC, an artificial magnetic conductor (AMC) is designed. It is equivalent to a magnetic conductor only in its operating band, and it behaves like a normal perfect electric conductor (PEC) outside the operating band. By taking advantage of this property, we can add a filtering function to the waveguide. By designing an AMC's operating band in the desired suppression band and loading it into the waveguide, the electromagnetic (EM) wave is cut off in the AMC's operating band. When combining two AMCs of different operating frequencies, a dual-stopband filtering function is obtained. Together with the radiating slots on the upper electric wall of the waveguide, a dual-stopband filtering antenna is achieved. The unit cell of the AMC is a cross-arm with four short stubs at the end. The advantage of this design is that the length and width of the arms and stubs can be controlled separately to accurately tune the operating frequency of the AMC. Fig. 3 shows the dispersion diagram of the waveguide loaded with the high-frequency AMC and low-frequency AMC. It can be observed that a bandgap of 11.1–12 GHz is formed by the high-frequency AMC in Fig. 3(a), and a bandgap of 8.17–9.2 GHz is formed by the low-frequency AMC in Fig. 3(b). Fig. 4 shows the equivalent circuit of the dual-stop band AMC-loaded waveguide slot array antenna. The AMC substrate is composed of a low-frequency AMC Z_L, a high-frequency AMC Z_H, and a junction Z_J that connects them. R_r is the radiation impedance of the slot. For the low-frequency AMC, C_{x1} is the capacitance between adjacent AMC stubs in the x-direction, L_{x1} the inductance between adjacent via-holes in the x-direction, C_{y1} the parallel capacitance of adjacent AMC stubs in the y-direction, and L_{y1} the parallel inductance of adjacent AMC via-holes in the y-direction. The high-frequency AMC circuit is modeled in the same way, containing the capacitances C_{x2}, C_{y2} and inductances L_{x2}, L_{y2}. For the AMC junction, C_J is the capacitance between adjacent AMC junctions in the x-direction, and L_J is the inductance of adjacent via holes in the x-direction.

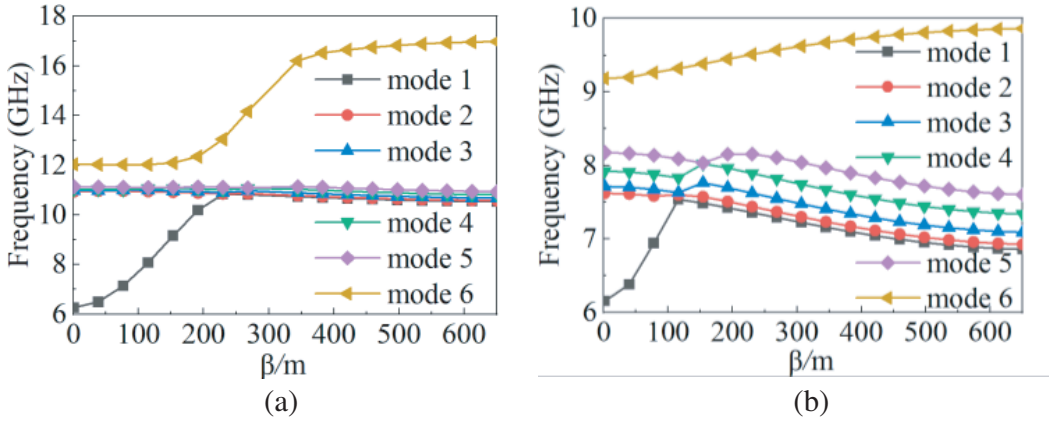

Figure 3. Dispersion diagram of the AMC-loaded waveguide: (a) high-frequency AMC and (b) low-frequency AMC.

To verify the above theory, two AMC substrates, which work at the desired high-frequency 10.75–11.5 GHz and low-frequency 8.09–9.10 GHz, are designed and loaded in the waveguide as shown in Fig. 2. The unit cell of the AMC is a cross-arm with four short stubs at the end. The advantage of this design is that the length and width of the arms and stubs can be controlled separately to accurately tune the operating frequency of the AMC. The simulated frequency response of the high-frequency AMC is shown in Fig. 5. It can be seen that the designed AMC shows a good stopband response and steep roll-off because of the strongly resonant structure. In the 10.75–11.5 GHz operating band, the transmission coefficient $|S_{21}|$ is lower than -35 dB, which implies a good bandstop characteristic. The roll-off is very steep, by which the transition from the stopband to the passband only takes up 0.17 GHz bandwidth. Fig. 6 shows the simulated frequency response of the high-frequency AMC versus its dimensions. The increase in the arm length reduces the distance between the stubs of adjacent AMC

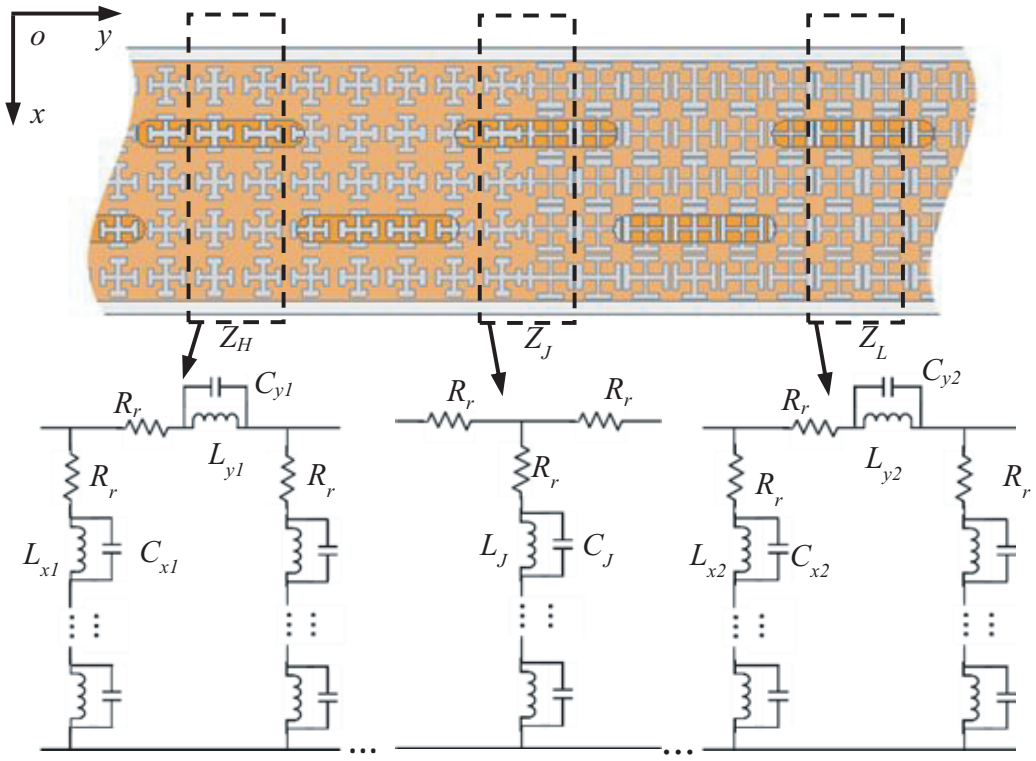

Figure 4. Equivalent circuit of the proposed antenna.

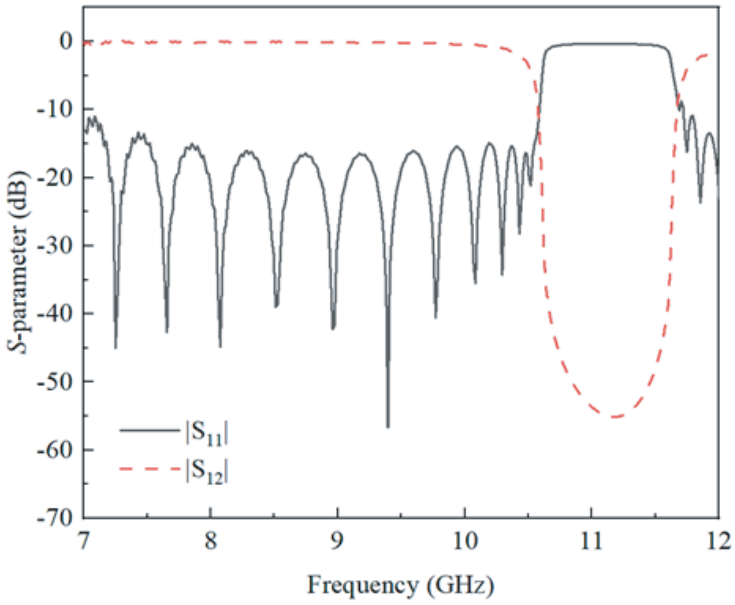

Figure 5. Simulated frequency response of the high-frequency AMC-loaded waveguide.

unit cells, which decreases the capacitances of C_{x1} and C_{y1} in Fig. 4 and shifts the operating frequency band to a lower frequency. An increase in the stub length increases the inductances L_{x1} and L_{y1} in Fig. 4, shifting the operating frequency to a lower band. In this design, we choose $l_1 = 3.7\,\text{mm}$ and $l_2 = 1.6\,\text{mm}$ for the high-frequency AMC to realize the high-frequency stopband. Ridges are designed

inside the waveguide to fix the AMC. The effect of the ridges is simulated. Fig. 7 gives a comparison of $|S_{21}|$ of AMC-loaded waveguide with and without ridges. It can be seen that for the relatively small dimensions of the ridges compared to the dominant guided wavelength, the addition of ridges changes the $|S_{21}|$ from -59 dB to -53 dB, while the center frequency and bandwidth are unaffected. Thus, the addition of the ridges does not affect the overall filtering performance. To verify the design, a waveguide prototype and a high-frequency AMC substrate are fabricated and measured. As shown in Fig. 8, the waveguide is made by the metallic 3D printing technology SLM, the high-frequency AMC substrate is made by PCB. Fig. 9 compares the measured and simulated results. The measured stopband is 10.77–11.5 GHz ($|S_{11}| > -0.5$), and the $|S_{11}|$ roll-off from -0.46 dB (10.77 GHz) to -11.6 dB (10.49 GHz)

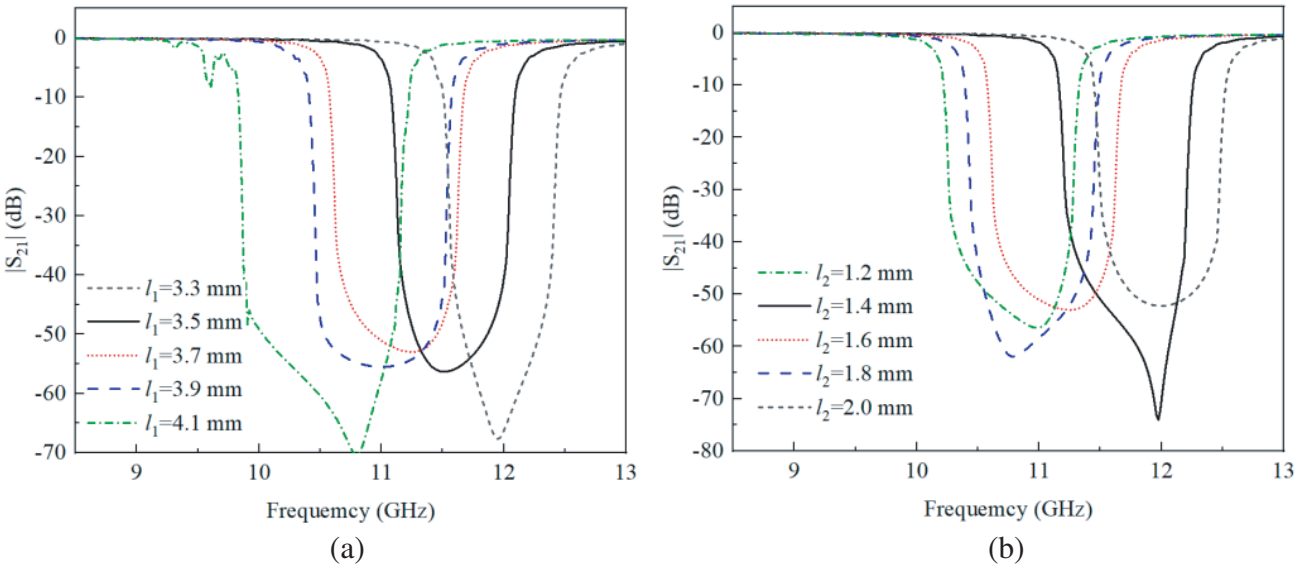

Figure 6. Simulated $|S_{21}|$ of the high-frequency AMC-loaded waveguide: (a) stub length l_1 as the variable and (b) arm length l_2 as the variable.

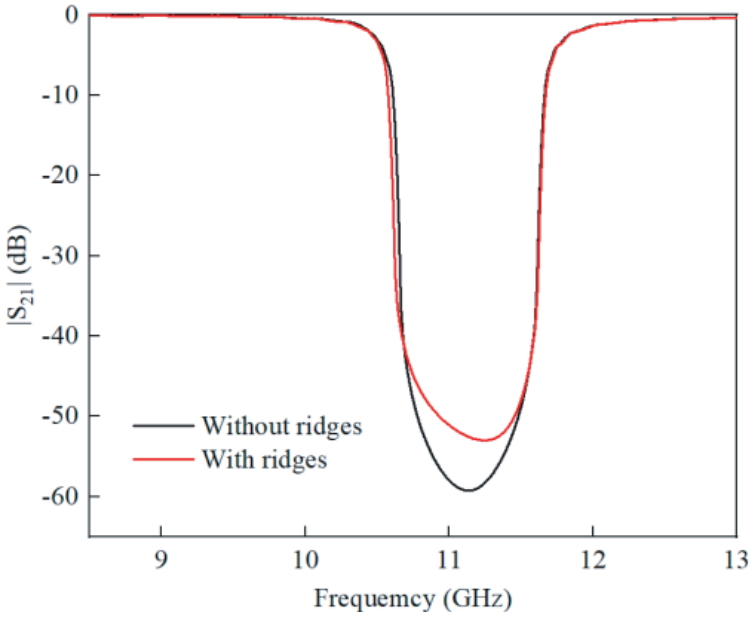

Figure 7. Simulated $|S_{21}|$ of the AMC-loaded waveguide with and without ridges.

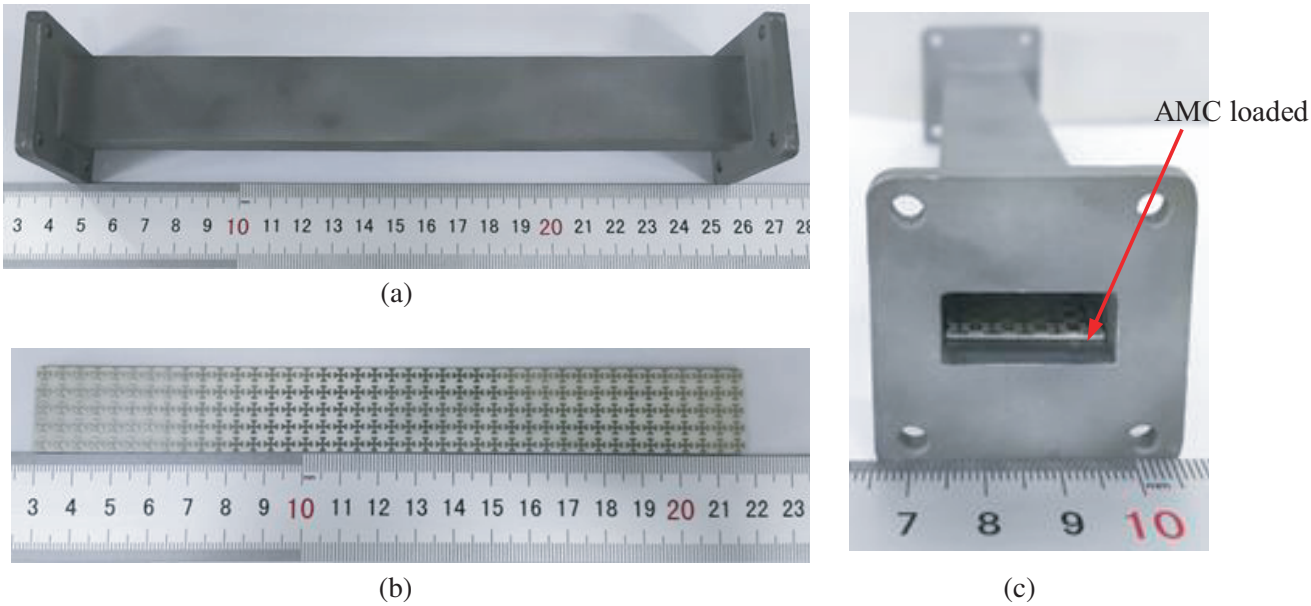

Figure 8. Photographs of the waveguide and the high-frequency AMC: (a) the waveguide, (b) the high-frequency AMC, and (c) the flange view of the AMC-loaded waveguide.

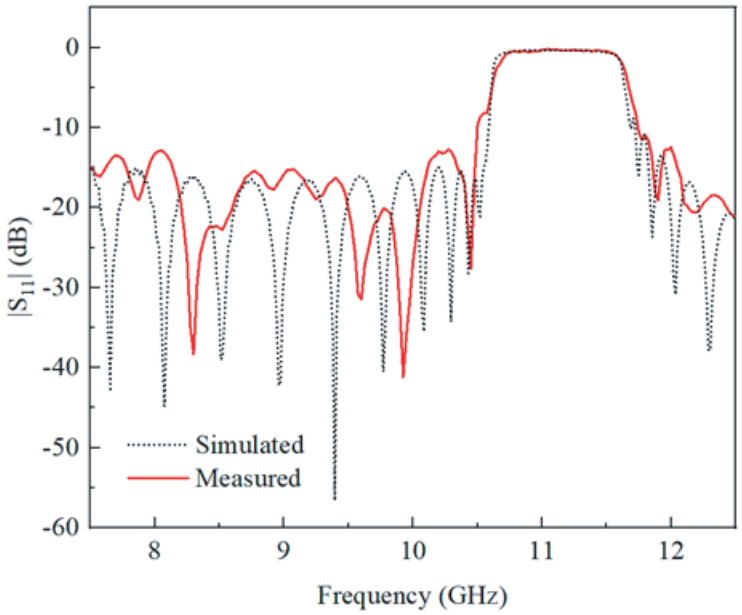

Figure 9. Simulated and measured $|S_{11}|$ of the high-frequency AMC-loaded waveguide.

within a bandwidth of 0.28 GHz. Compared with the simulation, the measured stopband is decreased by 0.02 GHz, and the $|S_{11}|$ roll-off region is increased by 0.11 GHz. This is due to the edge effect of the fabricated AMC. In the simulation, the AMC is modeled as an infinitely large periodical array of unit cells, while the array size is limited in reality. Thus, the weakened resonance on the edge of the AMC from its structural discontinuity leads to the deteriorated frequency response in measurement.

To realize the dual-stopband filtering effect, a low-frequency AMC is designed by scaling down the high-frequency AMC. A parametric study is performed to determine the arm length as $l_1 = 4.3$ mm

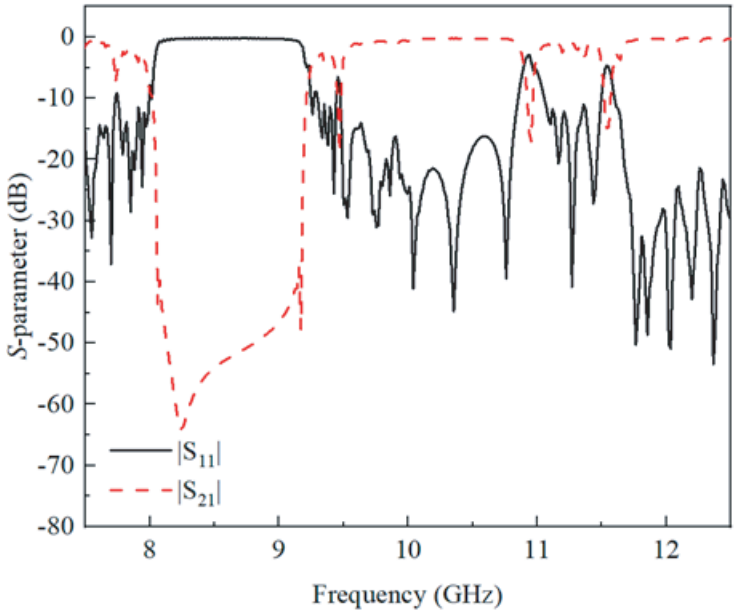

Figure 10. Simulated frequency response of the low-frequency AMC-loaded waveguide.

and $l_2 = 2.4$ mm to realize the low-frequency stopband. The simulated frequency response is shown in Fig. 10. The AMC works at 8.09–9.10 GHz. There are three dominant resonances at 9.44, 10.94, and 11.54 GHz. The resonance at 9.4 GHz can be eliminated by the slot radiation when the low-frequency AMC is loaded inside a waveguide slot array, which will be introduced in the following section. Parasitic behaviors at 10.94 and 11.54 GHz are caused by the mutual coupling between the short arms in the non-operating band of the low-frequency AMC. They fall into the stopband of the high-frequency AMC, which does not affect the filtering function of the proposed antenna.

2.3. Dual-Frequency AMC

By penalizing the high-frequency and low-frequency AMCs into a substrate, we expect to achieve a dual-stopband frequency response. Fig. 11 shows the simulated frequency response of the panelized dual-frequency AMC when it is loaded into a waveguide. It can be seen that a good dual-stopband characteristic is achieved, but significant resonances occur in the passband at 9.4 and 10.2 GHz. This is caused by the structural discontinuity between the high-frequency and low-frequency AMCs. On the panelized AMC substrate, which is equally divided into the high-frequency AMC zone on the left and the low-frequency AMC zone on the right, the high-frequency and low-frequency AMCs have no electric contact on their interface. As a result, the structural discontinuity causes multiple reflections, which is verified by the fluctuation of $|S_{11}|$ in the passband. Or from the perspective of the equivalent circuit model, the structural discontinuity introduces extra coupling capacitance which leads to multiple resonances in the passband. To achieve a smooth passband, the structural discontinuity or the coupling capacitance shall be eliminated. Hence, we connect the high-frequency AMC and low-frequency AMC with a section of microstrip line named 'AMC junction' in Fig. 2(b). This helps to realize a smooth transition from different structures. The inductance of the AMC junction also compensates for the coupling capacitance. The resonance at 10.2 GHz is eliminated by the AMC junction as shown in Fig. 12; however, the resonance at 9.4 GHz still exists. The 9.4 GHz resonance could be eliminated by the radiating slot, which will be introduced in the following part. A dual-frequency AMC substrate with an AMC junction is fabricated and measured to verify the function of the AMC junction. Fig. 13 shows a photograph of the fabricated dual-frequency AMC. It is loaded into the waveguide in Fig. 8 for testing. The simulated and measured $|S_{11}|$ agree well in Fig. 14. There is a slight frequency shift of the low-frequency resonance from 9.4 GHz to 9.6 GHz in the passband, which is caused by the fabrication

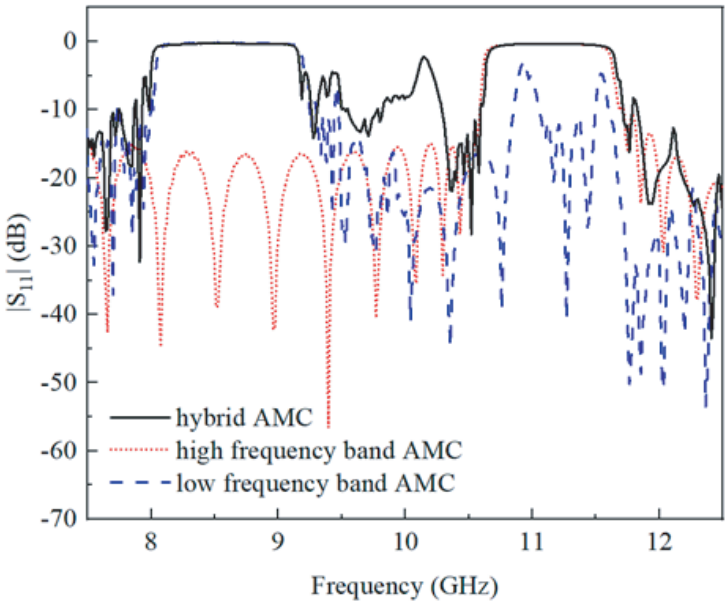

Figure 11. Simulated $|S_{11}|$ of the waveguide loaded with high-frequency AMC, low-frequency AMC, and dual-frequency AMC.

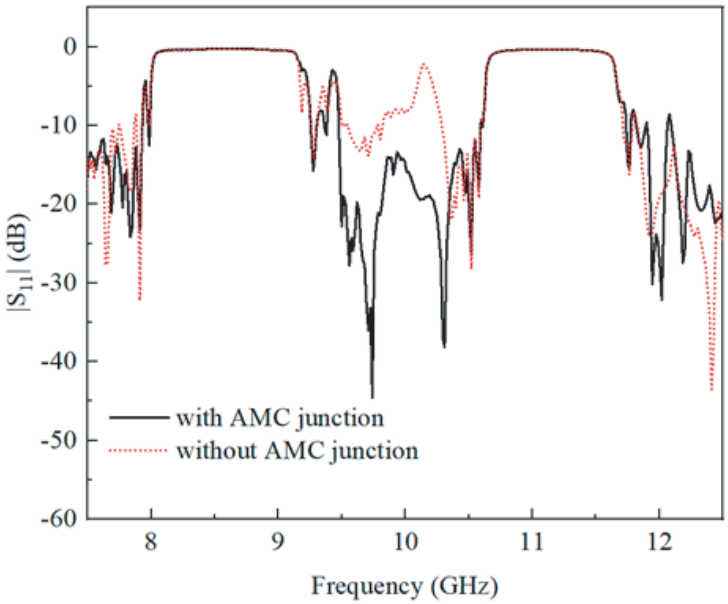

Figure 12. Simulated $|S_{11}|$ of the dual-frequency AMC with and without the junction.

tolerance. By introducing the AMC junction, the high-frequency resonance at 10.2 GHz in the passband is effectively removed.

2.4. The Filtering Antenna

A waveguide slot array is designed to be used together with the dual-frequency AMC to build a filtering antenna. The dual-frequency AMC demonstrates excellent bandpass characteristic except for the 9.4 GHz resonance in the passband in Fig. 14. Typical methods to get rid of the undesired resonance is either to introduce extra parasitic elements to shift the resonance to a different frequency

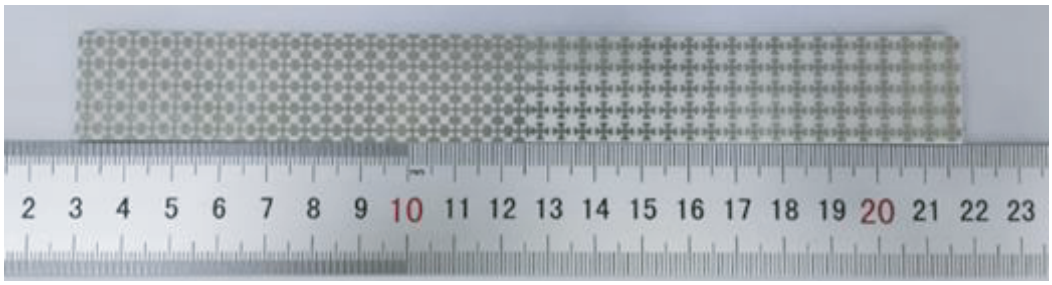

Figure 13. Photograph of the dual-frequency AMC with the junction.

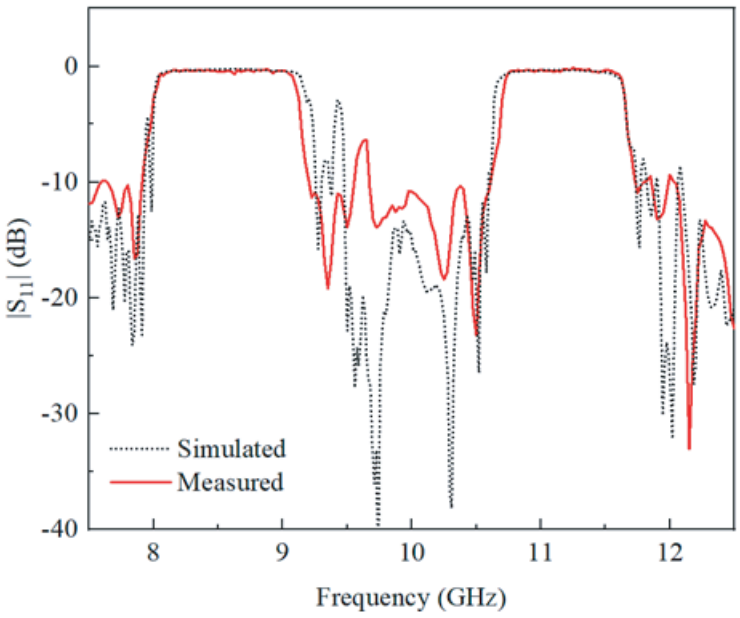

Figure 14. Simulated and measured $|S_{11}|$ of the dual-frequency AMC-loaded waveguide.

or to dissipate the resonant power. The former requires extra lump or discrete components to realize the required capacitance and inductance, which leads to increased system complexity and cost. The latter is applicable in our design, by which the resonant power is dissipated by the radiation resistance of the antenna, and no extra component is needed.

A uniform slot array is opened on the top electric wall of the dual-stopband AMC-loaded waveguide. Simulated S-parameters are shown in Fig. 15. It can be seen that the $|S_{11}|$ at 9.4 GHz drops below -10 dB, which proves that the resonant power is radiated into the free space through the slot while the filtering frequency response is not affected. From Fig. 15, it can be observed that the transmission coefficients of the two ports are the same, but the reflection coefficients are different, indicating that the proposed waveguide filtering antenna is reciprocal but not symmetric. Fig. 16 shows the radiation pattern at 9.8 GHz in the passband when different ports are excited. In the propagation constant analysis in Fig. 3, it can be calculated that propagation constants on the two AMCs at the same frequency are different. The different directions of the radiation pattern are caused by the variation of the propagation constant on the high-frequency and low-frequency AMCs. Since the slot array has a fixed element spacing, the variation of the propagation constant causes the change of the phase progression between array elements, and hence the beam direction changes. Fig. 17 depicts the simulated gain of the filtering antenna. The gain is 13.5 dBi and 11.8 dBi when ports 1 and 2 are excited, respectively. The reason for the asymmetric gain lies in the different propagation constants on the two AMCs. Even though

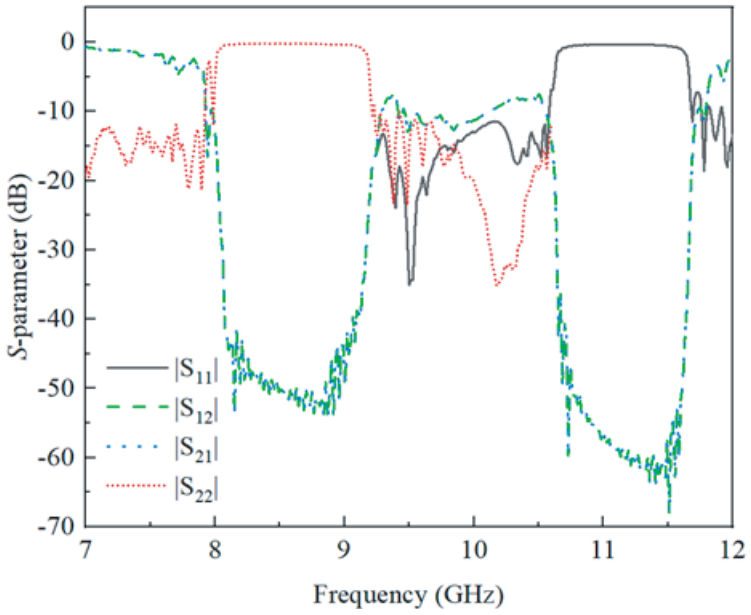

Figure 15. Simulated frequency response of the dual-frequency AMC-loaded waveguide slot array.

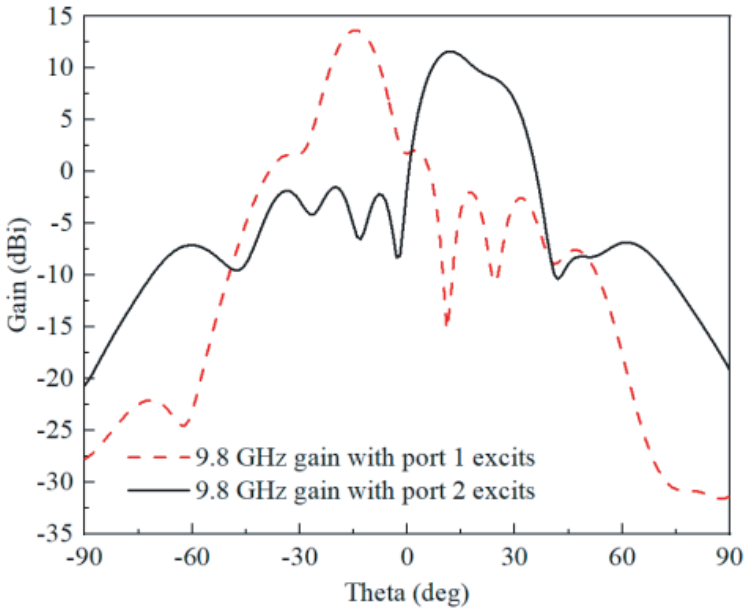

Figure 16. Simulated radiation patterns when port 1 and port 2 excite at 9.8 GHz in the passband.

the slots have uniform dimensions, they exhibit different radiation resistances when the propagation constant varies. As a traveling wave antenna, most of the input power is radiated into free space from slots near the input port. It can be calculated that the radiation resistance of the slots near port 1 when port 1 is excited is larger than the radiation resistance of the slots near port 2 when port 2 is excited. As a result, a decreased gain is observed when port 2 is excited. This also accounts for the asymmetric input impedance in Fig. 15 and asymmetric radiation patterns in Fig. 16. The radiation efficiency and total efficiency of the antenna when ports 1 and 2 are excited are given in Fig. 18. It can be seen that the radiation efficiency of the proposed antenna is above 80% in the operating band with the maximum radiation efficiency of 96%, and the total efficiency is 10% below radiation efficiency. The desirable

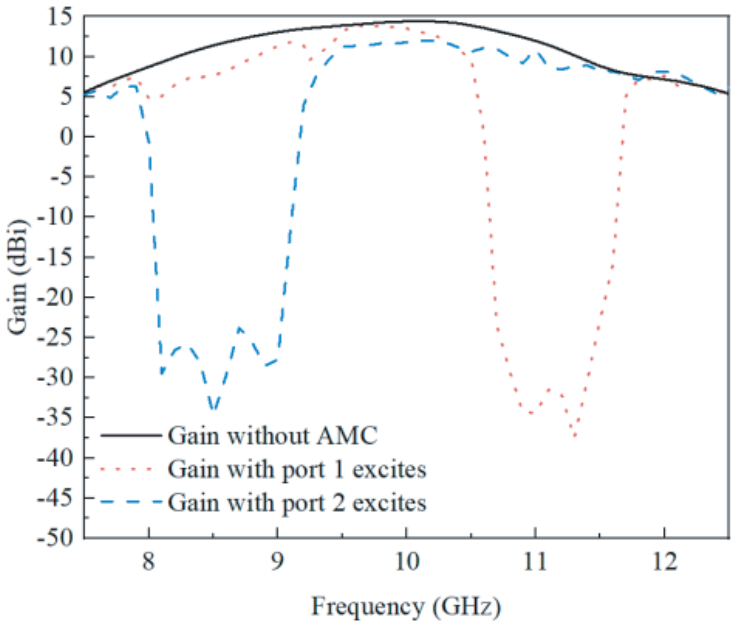

Figure 17. Simulated gain of the dual-frequency AMC-loaded waveguide slot array when port 1 and port 2 excite.

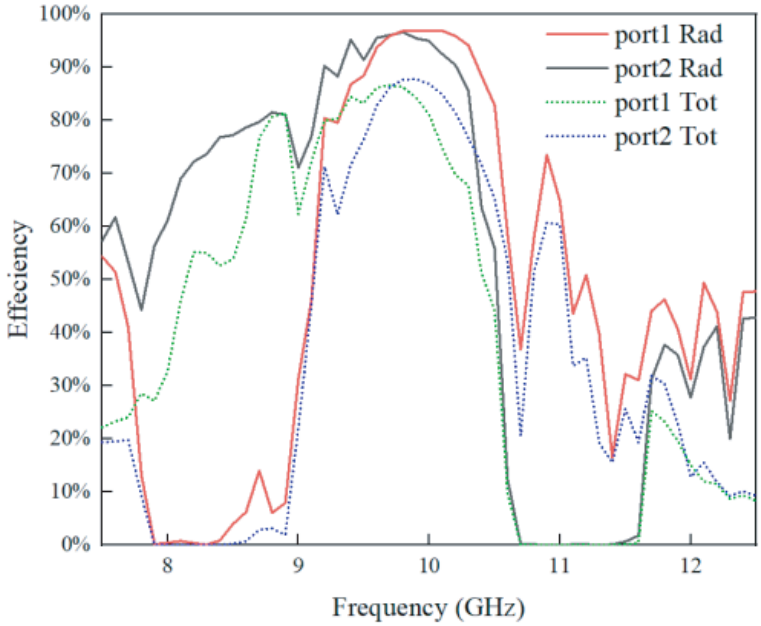

Figure 18. Radiation efficiency of the proposed antenna.

radiation efficiency of the proposed antenna is from the low loss characteristic of the waveguide and the AMC substrate.

3. FABRICATION AND MEASUREMENT

To verify the design concept, an X-band AMC-loaded waveguide slot array filtering is fabricated and tested. The CST Microwave Studio is used for simulation. The antenna is tested in the near-field measurement setup at Sichuan University. As shown in Fig. 19(a), the waveguide slot array antenna

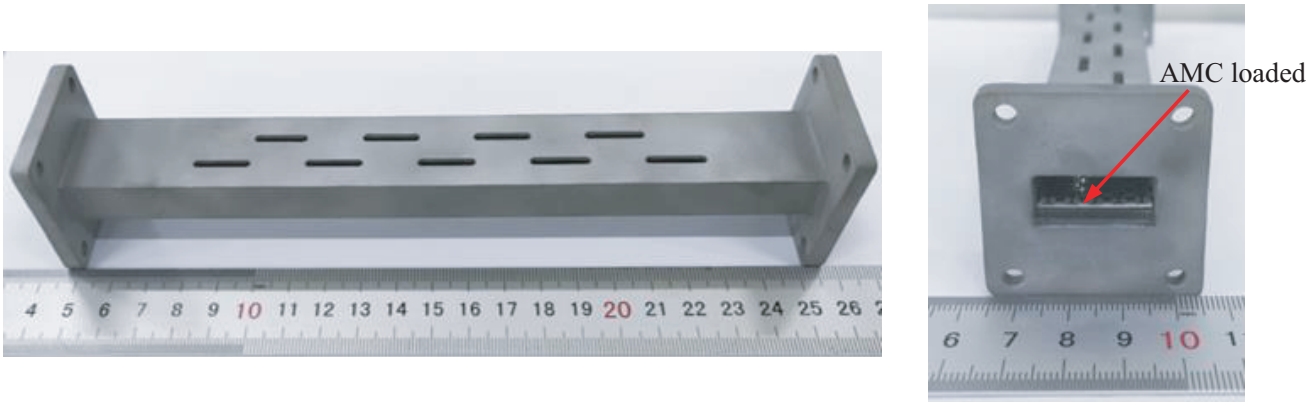

Figure 19. Photographs of the fabricated AMC-loaded waveguide slot array antenna: (a) the waveguide slot array and (b) the flange view of the AMC-loaded waveguide slot array antenna.

is made by SLM using aluminum alloy in one piece in one run, saving the effort of assembly and post-processing. The AMC substrate can be inserted and removed easily as shown in Fig. 19(b). The ridges near the flange ensure that the AMC has good contact with the bottom electric wall of the waveguide. The ridges also help to avoid the substrate from buckling and protruding during insertion.

Figure 20 depicts the simulated and measured S-parameters of the proposed antenna. The measured and simulated results agree well. It has two stopbands of 8.1–9 GHz and 10.75–11.5 GHz. The passband is 9.25–10.6 GHz. There is a slight difference between the simulated and measured stopbands, which is caused by the manufacturing tolerance. The roll-off from the stopband to the passband is very steep. The transition band from the high-frequency stopband to the passband occupies only 0.15 GHz, and there is no ripple during the roll-off. The transition from the low-frequency stopband to the passband occupies 0.25 GHz, and the roll-off is still very steep, although the processing error leads to a small

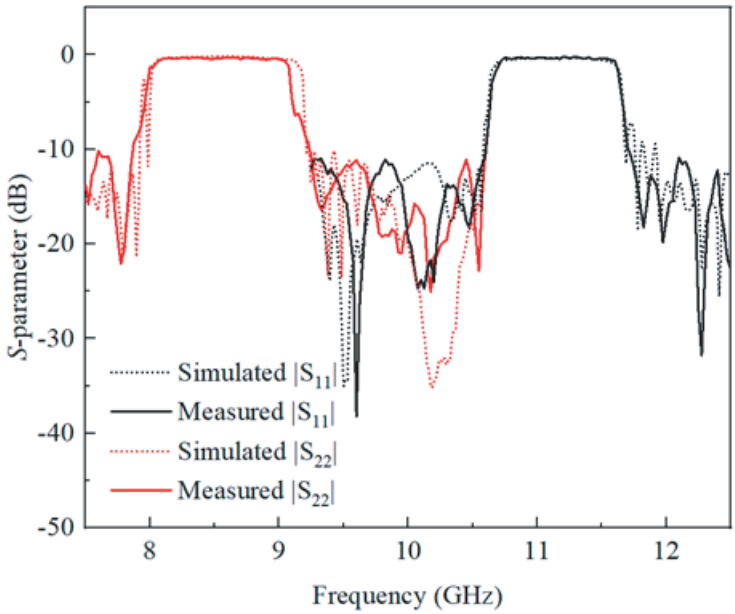

Figure 20. Simulated and measured frequency response of the AMC-loaded waveguide slot array antenna.

ripple. The dual-stopband frequency response with steep roll-off can ensure good isolation between the receiver and transmitter in a radar system.

Figure 21 gives the measured gain of the proposed antenna when different ports are excited. Agreement is achieved between simulation and measurement. When port 1 is excited, in the passband the maximum gain of 13.51 dBi is observed at 9.7 GHz with a 3-dB gain bandwidth of 9.3–10.4 GHz. When port 2 is excited, the maximum gain of 11.46 dBi is observed at 10 GHz in the passband with the 3-dB gain bandwidth of 9.2–10.7 GHz. The average gain rejection is 35 dB and 43 dB in the low-frequency and high-frequency stopbands respectively with the highest gain rejection up to 50 dB. When different ports are excited, guided wave wavelengths are different due to the propagation constants of the low-frequency and high-frequency AMCs. As the length of the radiation slot is constant, the radiation resistance of the slot differs when different ports are excited, resulting in a different port gain. As the element spacing is constant, the phase progression is also different when different ports are excited, which leads to the asymmetry of the beam direction. The reciprocity of the proposed filtering antenna is still acceptable in terms of gain.

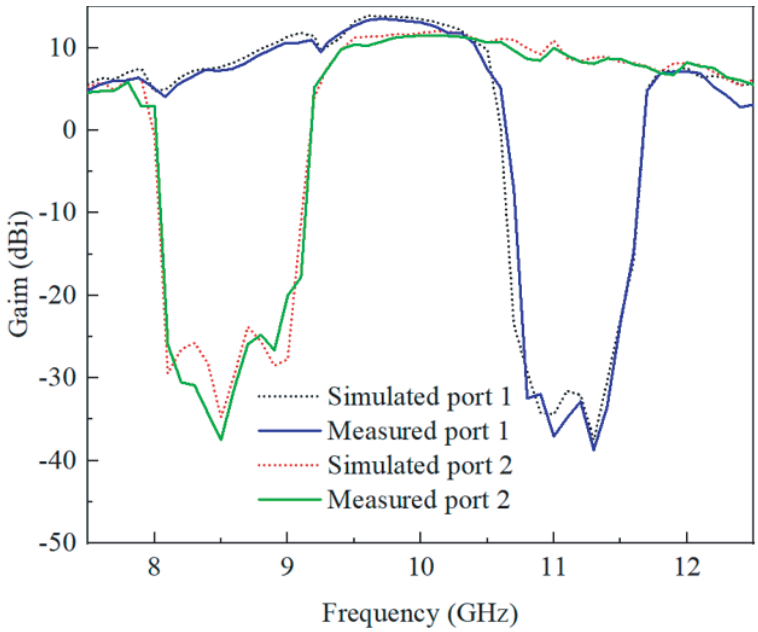

Figure 21. Simulated and measured gain of the AMC-loaded waveguide slot array antenna.

As a traveling wave antenna, the proposed antenna features frequency-dependent radiation patterns. Fig. 22 shows the simulated and measured H-plane radiation patterns when port 1 and port 2 are excited at 9.5 GHz, 9.8 GHz, 10.1 GHz, and 10.4 GHz, respectively. When port 1 is excited, the radiation pattern points at −19.5, −14, −11.5, and −6.5 degrees at 9.5 GHz, 9.8 GHz, 10.1 GHz, and 10.4 GHz in Figs. 22(a), (c), (e), and (g). When port 2 is excited, the radiation pattern points at 15, 11.5, 8.5, and 5.5 degrees at 9.5 GHz, 9.8 GHz, 10.1 GHz, and 10.4 GHz in Figs. 22(b), (d), (f), and (h). The difference between the simulated and measured direction of patterns is caused by the vibration in measurement. The distortion of the measured radiation pattern is caused by the fabrication tolerance on the radiating slot. The surface roughness on the edges of the radiating slot causes diffraction of the radiated power, which leads to the distortion of the antenna's aperture field distribution, and thus distorted radiation patterns.

Figure 23 shows the simulated and measured E-plane radiation patterns when port 1 and port 2 are excited. Measurement and simulation agree well. Table 2 compares the proposed filtering antenna with other reported works. Different from the antennas in [28–30], which realize the filtering response by implementing complex machined cavities inside the waveguide, the proposed antenna achieves the filtering response in the waveguide by loading the planar AMC processed by PCB technology. Therefore,

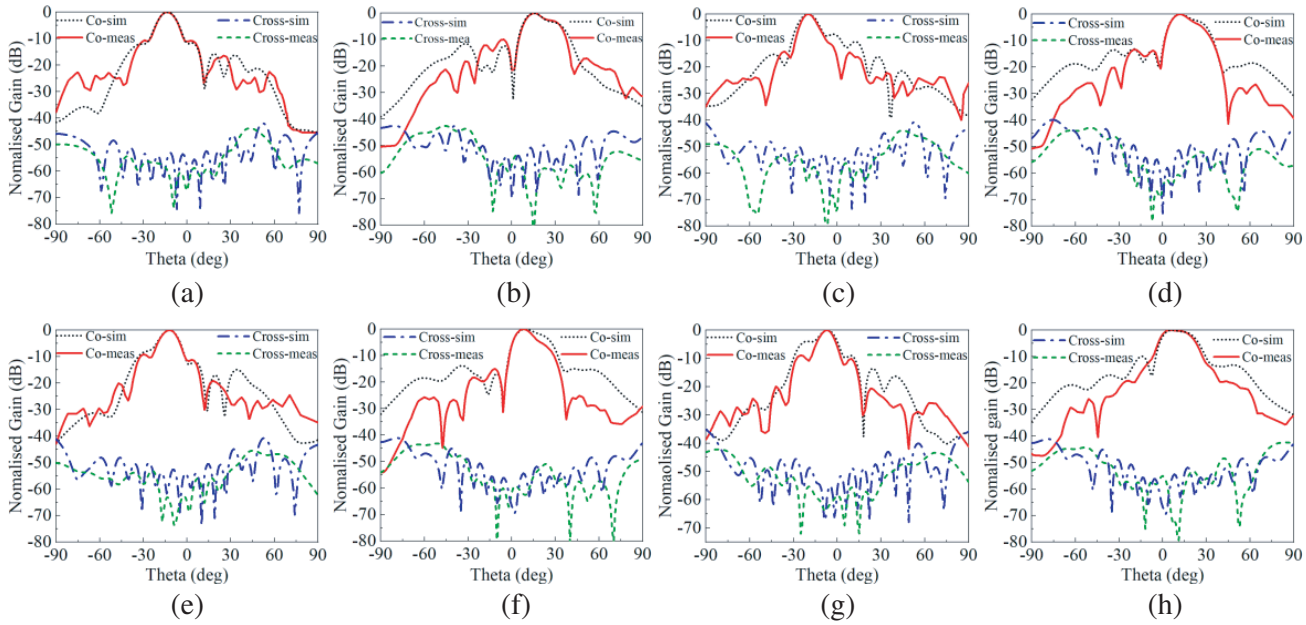

Figure 22. Simulated and measured H-plane radiation patterns of the AMC-loaded waveguide slot array antenna: (a) port 1 excites at 9.5 GHz, (b) port 2 excites at 9.5 GHz, (c) port 1 excites at 9.8 GHz, (d) port 2 excites at 9.8 GHz, (e) port 1 excites at 10.1 GHz, (f) port 2 excites at 10.1 GHz, (g) port 1 excites at 10.4 GHz, and (h) port 2 excites at 10.4 GHz.

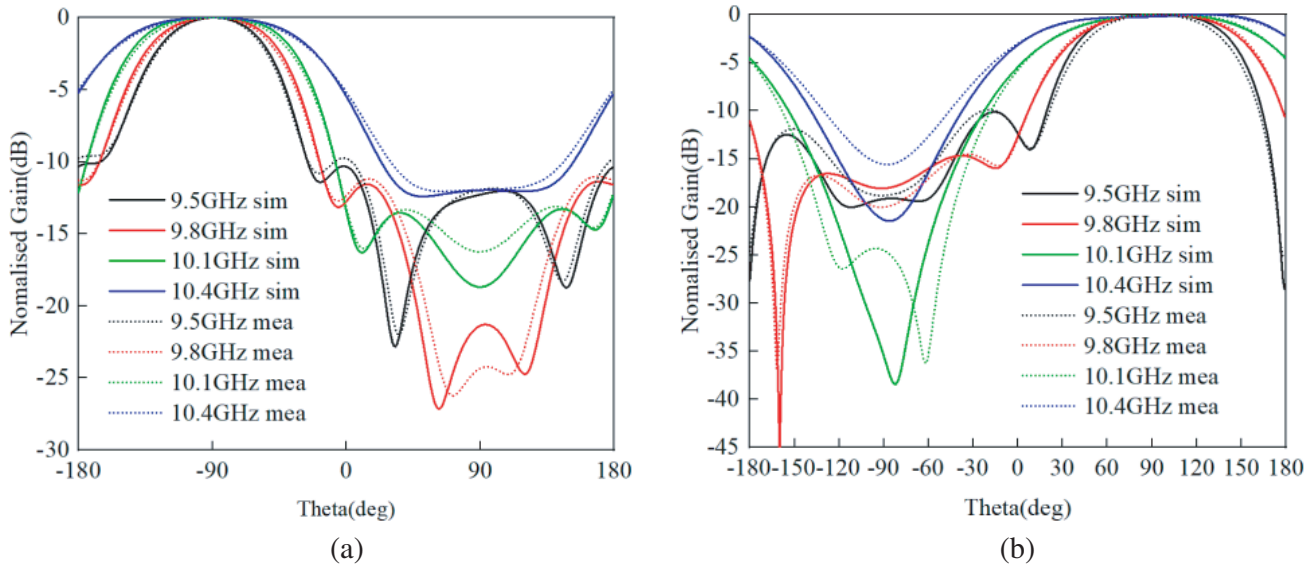

Figure 23. Simulated and measured E-plane radiation patterns of the AMC-loaded waveguide slot array antenna: (a) port 1 excites, (b) port 2 excites.

the proposed antenna outstands with a significant reduction in the manufacturing cost. Though the counterparts have good out-of-band rejection, they only have a single stopband. Comparatively, the proposed antenna has a dual-stopband with a steep roll-off. With the steep roll-off dual-stopband and interchangeable modularized design, the proposed antenna is a good choice for a highly integrated airborne radar system.

Table 2. Comparison between filtering antennas.

Ref.	Passband (GHz)	Dual stopband	Roll-off (dB/GHz)	Out-of-band rejection (dB)	Beam scanning	Gain (dBi)
[28]	12.25–12.75	No	7.2	14.8–21.3	No	15.82
[29]	5.3–5.7	No	3.6	> 35	No	12.2
[30]	12.1–12.8	No	8.1	> 40	No	13.6
This work	9.25-10.6	Yes	40 and 67	> 35	Yes	13.5

4. CONCLUSION

In this paper, an AMC-loaded dual-stopband filtering waveguide slot array antenna is designed. When the waveguide's cutoff frequency coincides with the operational frequencies of the AMC, two stopbands are formed, and a passband is achieved between the two stopbands. The steep roll-off frequency response of the AMC endows the filtering antenna with better than 35 dB out-of-band rejection. Since the frequency response of the filtering antenna is dependent upon that of the AMC, the proposed design concept can theoretically achieve arbitrary frequency response by just inserting different AMCs into the waveguide. The interchangeable modularized design effectively increases the level of system integration and reduces the assembly cost of the radar system. Using PCB and metallic 3D printing technologies to fabricate the AMC and the waveguide slot array respectively helps to reduce the fabrication cost and turn-around time of product prototyping. The proposed filtering antenna is a desirable antenna choice for high-power airborne radar applications. The power limit depends on the capacity of the AMC substrate. The design concept is instructive for engineers to achieve a low-cost, compact, and frequency response reconfigurable filtering antenna.

ACKNOWLEDGMENT

This work is supported by the National Natural Science Foundation of China under grant 62171301, by the State Key Laboratory of Millimeter Waves under grant K202322, and by the State Key Laboratory of Polymer Materials Engineering under grant sklpme 2022-2-03. The authors acknowledge the financial support from the National Natural Science Foundation of China under grant 62171301 and from the State Key Laboratory of Polymer Materials Engineering under grant sklpme 2002-2-03.

APPENDIX A.

For a classic rectangular waveguide, the cutoff frequency and electric field distribution can be calculated by Maxwell's equations and boundary conditions. Taking its long side as the x-axis and the short side as the y-axis, the general solution of the propagation function h_z of the TE mode can be obtained as follows

$$h_z(x, y) = (A \cos k_x x + B \sin k_x x)(C \cos k_y y + D \sin k_y y) \tag{A1}$$

Combined with the boundary condition of four perfect electric conductors (PECs) walls, we can get that the electric field in the x-direction is 0 when y equals 0 and b, and the electric field in the y-direction is 0 when x equals 0 and a. We can solve for $B = 0$ and $D = 0$ in Eq. (A1), so the final solution of H_z is

$$H_z(x, y, z) = A_{mn} \cos \frac{m\pi x}{a} \cos \frac{n\pi y}{b} e^{-j\beta z} \tag{A2}$$

As the boundary condition of the bottom wall changes from PEC to perfect magnetic conductor (PMC), the electric field in the y direction is 0 when x equals 0 and a; the electric field in the x direction is 0

when y equals b; and the magnetic field in the x direction is 0 when y equals 0. Expressions for the electric and magnetic fields in the x- and y-directions are given in Eqs. (A3)–(A6)

$$h_x = \frac{-j\beta}{k_c^2} k_x(-A\sin k_x x + B\cos k_x x)(C\cos k_y y + D\sin k_y y) \tag{A3}$$

$$h_y = \frac{j\beta}{k_c^2} k_y(A\cos k_x x + B\sin k_x x)(-C\sin k_y y + D\cos k_y y) \tag{A4}$$

$$e_x = \frac{-j\omega\mu}{k_c^2} k_y(A\cos k_x x + B\sin k_x x)(-C\sin k_y y + D\cos k_y y) \tag{A5}$$

$$e_y = \frac{j\omega\mu}{k_c^2} k_x(-A\sin k_x x + B\cos k_x x)(C\cos k_y y + D\sin k_y y) \tag{A6}$$

Bringing the boundary condition into Eqs. (A3)–(A6), we can calculate $B = 0$ and $C = 0$. Then bringing the results into Eq. (A1), we can obtain the final solution of the magnetic field intensity in the z-direction in the waveguide with the bottom wall as PMC as follows

$$H_z(x, y, z) = A_{mn}\cos\frac{m\pi x}{a}\sin\frac{(2n+1)\pi y}{2b}e^{-j\beta z} \tag{A7}$$

The cutoff frequency of the PMC-loaded waveguide can be calculated as

$$f_c = \frac{1}{2\pi\sqrt{\mu\varepsilon}}\sqrt{\left(\frac{m\pi}{a}\right)^2 + \left(\frac{(2n+1)\pi}{2b}\right)^2} \tag{A8}$$

REFERENCES

1. Ziolkowski, R. and A. Erentok, "Metamaterial-based efficient electrically small antennas," *IEEE Trans. Antennas Propag.*, Vol. 54, No. 7, 2113–2130, Jul. 2006.
2. Ma, X., C. Huang, W. Pan, B. Zhao, J. Cui, and X. Luo, "A dual circularly polarized horn antenna in Ku-band based on chiral metamaterial," *IEEE Trans. Antennas Propag.*, Vol. 62, No. 4, 2307–2311, Apr. 2014.
3. Zhang, N., W. X. Jiang, H. F. Ma, W. X. Tang, and T. J. Cui, "Compact high-performance lens antenna based on impedance-matching gradient-index metamaterials," *IEEE Trans. Antennas Propag.*, Vol. 67, No. 2, 1323–1328, Feb. 2019.
4. Zhang, S., R. Arya, W. Whittow, D. Cadman, R. Mittra, and J. Vardaxoglou, "Ultra-wideband flat metamaterial GRIN lenses assisted with additive manufacturing technique," *IEEE Trans. Antennas Propag.*, Vol. 69, No. 7, 3788–3799, Jul. 2021.
5. Kuester, E., M. Mohamed, M. Piketmay, and C. Holloway, "Averaged transition conditions for electromagnetic fields at a metafilm," *IEEE Trans. Antennas Propag.*, Vol. 51, No. 10, 2641–2651, Oct. 2003.
6. Holloway, C., M. Mohamed, E. Kuester, and A. Dienstfrey, "Reflection and transmission properties of a metafilm: With an application to a controllable surface composed of resonant particles," *IEEE Trans. Antennas Propag.*, Vol. 47, No. 4, 853–865, Nov. 2005.
7. Holloway, C., A. Dienstfrey, E. Kuester, J. O'Hara, A. Azad, and A. Taylor, "A discussion on the interpretation and characterization of metafilms/metasurfaces: The two-dimensional equivalent of metamaterials," *Metamaterials*, Vol. 3, No. 2, 100–112, Oct. 2009.
8. Holloway, C., E. Kuester, and A. Dienstfrey, "Characterizing metasurfaces/metafilms: The connection between surface susceptibilities and effective material properties," *IEEE Antennas Wireless Propag. Lett.*, Vol. 10, 1507–1511, 2011.
9. Mehdipour, A., J. Wong, and G. Eleftheriades, "Beam-squinting reduction of leaky-wave antennas using Huygens metasurfaces," *IEEE Trans. Antennas Propag.*, Vol. 63, No. 3, 978–992, Mar. 2015.
10. Vallecchi, A., J. Luis, F. Capolino, and F. Flaviis, "Low profile fully planar folded dipole antenna on a high impedance surface," *IEEE Trans. Antennas Propag.*, Vol. 60, No. 1, 51–62, Jan. 2012.

11. Vellucci, S., A. Monti, M. Barbuto, G. Oliveri, et al., "On the use of nonlinear metasurfaces for circumventing fundamental limits of mantle cloaking for antennas," *IEEE Trans. Antennas Propag.*, Vol. 69, No. 8, 5048–5053, Aug. 2021.
12. Yang, W., S. Chen, W. Che, Q. Xue, and Q. Meng, "Compact high-gain metasurface antenna arrays based on higher-mode SIW cavities," *IEEE Trans. Antennas Propag.*, Vol. 66, No. 9, 4918–4923, Sep. 2018.
13. Gu, L., W. Yang, Q. Xue, and W. Che, "A dual-band steerable dual-beam metasurface antenna based on common feeding network," *IEEE Trans. Antennas Propag.*, Vol. 69, No. 10, 6340–6350, Oct. 2021.
14. Herruzo, J., M. Rocher, A. Nogueira, and B. Clemente, "Novel asymmetric T-shaped radiating element for circularly-polarized waveguide slot arrays," *IEEE Trans. Antennas Propag.*, Vol. 69, No. 11, 7452–7461, Nov. 2021.
15. Wu, X., F. Yang, F. Xu, and J. Zhou, "Circularly polarized waveguide antenna with dual pairs of radiation slots at Ka-band," *IEEE Antennas Wireless Propag. Lett.*, Vol. 16, 2947–2950, Sep. 2017.
16. Liu, Y., X Liang, X. Zhang, et al., "A K-band broadband circularly polarized slot antenna based on L-shaped waveguide cavity," *IEEE Antennas Wireless Propag. Lett.*, Vol. 20, No. 9, 1606–1610, Sep. 2021.
17. Li, T., H. Meng, and W. Dou, "Design and implementation of dual-frequency dual-polarization slotted waveguide antenna array for *Ka*-band application," *IEEE Antennas Wireless Propag. Lett.*, Vol. 13, 1317–1320, Jul. 2014.
18. Chen, M., X. Fang, W. Wang, H. Zhang, and G. Huang, "Dual-band dual-polarized waveguide slot antenna for SAR applications," *IEEE Antennas Wireless Propag. Lett.*, Vol. 19, No. 10, 1719–1723, Oct. 2020.
19. Chen, J., T. Hu, Y. Zhao, L. Li, et al., "Realization of the high-gain low-sidelobe wide-sector beam using inductive diaphragms loaded slotted ridge waveguide antenna array for air detection applications," *IEEE Trans. Antennas Propag.*, Vol. 70, No. 4, 2698–2707, Apr. 2022.
20. Wu, M., B. Zhang, Y. Zhou, and K. Huang, "A double-fold 7×8 butler matrixfed multibeam antenna with a boresight beam for 5G applications," *IEEE Antennas Wireless Propag. Lett.*, Vol. 21, No. 3, 516–520, Mar. 2022.
21. Liu, J. and B. Zhang, "A modularized interchangeable multibeam slot array antenna using hybrid substrates for mass production," *IEEE Antennas Wireless Propag. Lett.*, Vol. 20, No. 5, 723–727, May 2021.
22. Cheng, Y. and Y. Dong, "A shared-aperture dual-band high-efficiency antenna based on groove gap waveguide," *IEEE Antennas Wireless Propag. Lett.*, Vol. 21, No. 8, 1620–1624, Aug. 2022.
23. Wu, Y., Z. Hao, Z. Miao, W. Hong, and J. Hong, "A 140 GHz high-efficiency slotted waveguide antenna using a low-loss feeding network," *IEEE Antennas Wireless Propag. Lett.*, Vol. 19, No. 1, 94–98, Jan. 2020.
24. Herruzo, J., A. Nogueira, M. Rocher, and B. Clemente, "High-efficiency Ka-band circularly polarized radial-line slot array antenna on a bed of nails," *IEEE Trans. Antennas Propag.*, Vol. 70, No. 5, 3343–3353, May 2022.
25. Kim, D., Y. Lim, H. Yoon, and S. Nam, "High-efficiency W-band electroforming slot array antenna," *IEEE Trans. Antennas Propag.*, Vol. 63, No. 4, 1854–1857, Apr. 2015.
26. Xu, X., M. Zhang, J. Hirokawa, and M. Ando, "*E*-band plate-laminated waveguide filters and their integration into a corporate-feed slot array antenna with diffusion bonding technology," *IEEE Trans. Microwave Theory Tech.*, Vol. 64, No. 11, 3592–3603, Nov. 2016.
27. Lu, J., H. Zhang, W. Wang, et al., "Broadband dual-polarized waveguide slot filtenna array with low cross polarization and high efficiency," *IEEE Trans. Antennas Propag.*, Vol. 67, No. 1, 151–159, Jan. 2019.
28. Yuan, W., X. Liang, L. Zhang, J. Geng, W. Zhu, and R. Jin, "Rectangular grating waveguide slot array antenna for SATCOM applications," *IEEE Trans. Antennas Propag.*, Vol. 67, No. 6, 3869–3880, Jun. 2019.

29. Wang, W., Z. Zheng, X. Fang, et al., "A waveguide slot filtering antenna with an embedded metamaterial structure," *IEEE Trans. Antennas Propag.*, Vol. 67, No. 5, 2953–2960, May 2019.
30. Zheng, Z., X. Fang, W. Wang, G. Huang, H. Zhang, and X. Liang, "A compact waveguide slot filtering antenna based on mushroom-type surface," *IEEE Antennas Wireless Propag. Lett.*, Vol. 19, No. 10, 1823–1827, Oct. 2020.